Experimental investigation on the fatigue and fracture properties of a fine pearlitic rail steel

D. Leonetti
Eindhoven University of Technology, The Netherlands
d.leonetti@tue.nl, https://orcid.org/0000-0002-7436-3977

B. Schotsman
Delft University of Technology, The Netherlands
ProRail, The Netherlands
b.schotsman@tudelft.nl, http://orcid.org/ 0000-0001-6174-2954

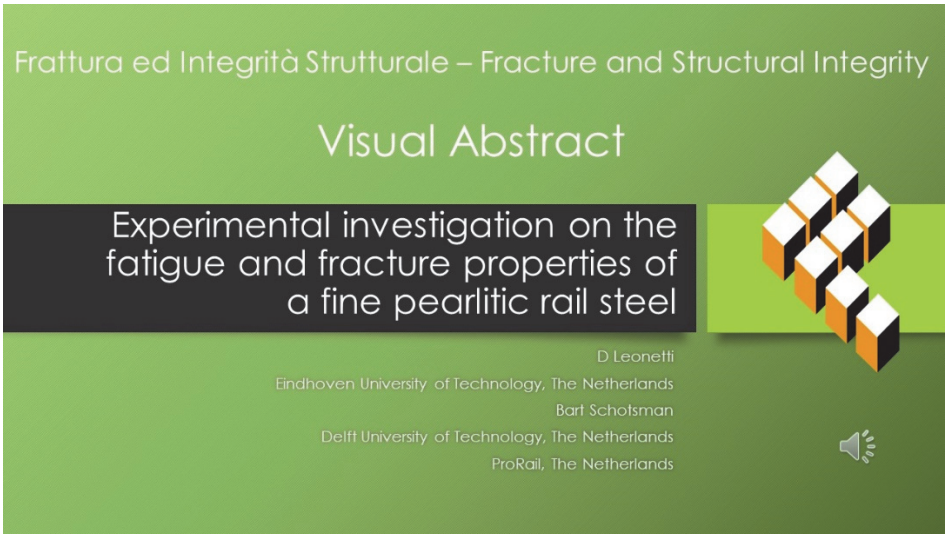

Citation: Leonetti, D., Schotsman, B., Experimental investigation on the fatigue and fracture properties of a fine pearlitic rail steel, Frattura ed Integrità Strutturale, 69 (2024) 142-153.

Received: 31.01.2024
Accepted: 14.04.2024
Published: 27.04.2024
Issue: 07.2024

Copyright: © 2024 This is an open access article under the terms of the CC-BY 4.0, which permits unrestricted use, distribution, and reproduction in any medium, provided the original author and source are credited.

KEYWORDS. R350HT rail steel, Fatigue Crack Growth, Rotating Bending, Fracture Toughness.

INTRODUCTION

The increasing traffic load and intensity on the railway network requires the use of high-strength and wear-resistant rail steels, to guarantee the safe use of the rail infrastructure. Rails are subjected to localized and high contact forces, inducing slipping mechanisms, and adverse weather conditions, causing wear, rolling contact fatigue, and other rail-related damage phenomena [1,2].

As a result of the shift to steel grades characterized by higher strength and wear resistance, rolling contact fatigue cracks are more likely to initiate, potentially leading to fatigue failure, determining a competition between these two phenomena, i.e. rolling contact fatigue and wear. It has been noted that the accumulation of plastic strain is the reason for both [3,4].
Continuous optimization of the chemical composition and production methods of railway steels aims to improve the strength, toughness, and resistance against wear. As an example, R350HT is a steel grade that is largely employed in switches, crossings, and curved tracks because of its increased strength. As compared to standard-grade (R260), R350HT is cooled faster after hot rolling, resulting in a smaller interlamellar spacing of the pearlitic structure, resulting in increased hardness and strength.
Railway rails are subjected to rolling contact fatigue, therefore, characterization of the resistance to crack initiation, crack growth and final fracture is highly relevant [5,6]. Concerning this, several methods and models have been developed to estimate the severity of the stress state at the tip of fatigue cracks, formulating finite element models, or weight function solutions [6-12]. It is well known that pearlitic steels are characterized by a brittle behavior under quasi-static loading conditions at room temperature [13]. This generally results in relatively low damage tolerance properties, i.e. relatively high fatigue crack growth rate and low fracture toughness at the service temperature [5].
On the contrary, monotonic tensile stress-strain curves and S-N curves are such that static and fatigue strength properties related to crack initiation can be qualified as relatively high [14], since rail steels have, at the rail surface, Brinell Hardness values, between 260 and 400 HB.
The study of the fracture behavior through the investigation of the fracture surfaces supports the further development of rail steels. Therefore, characterizing the fracture resistance in terms of fatigue crack growth and fracture toughness of rails steels allows us to assess the damage tolerance of railway rails. This paper shows a dedicated experimental investigation on R350HT rail steel. In particular, reference is made to monotonic tensile tests that have been conducted on coupons extracted from the rail head and reported in ref. [15]. In addition, linear elastic plane strain fracture toughness tests and fatigue crack growth rate tests have been conducted to quantify fracture mechanics properties and compare them with similar steel grades. Rotating bending tests are conducted to quantify the resistance to crack initiation. Moreover, the fracture surfaces are inspected to quantify and investigate the mechanisms underlying stable and unstable crack growth, as well as the tortuosity of the fracture surfaces through measurements conducted at a confocal microscope.

MATERIALS AND METHODS

The experimental program is performed on specimens extracted from new rails of R350HT railway steel, with a 60 kg/m profile conforming the EN13674-1 [16]. The R350HT rail steel is a fine pearlitic steel having a close-to-eutectoid chemical composition as shown in Tab. 1. The rail is hot-rolled and the fine pearlite results from accelerated cooling. The Vickers hardness of the undeformed microstructure is 355 ± 8 HV. All specimens are extracted from the same batch of material.

	C	Mn	Si
R350HT	0.77	1.10	0.39

Table 1: Chemical composition of the R350HT rail steel grade (wt%).

Monotonic tensile tests

The monotonic tensile tests summarized in this work have been presented in [15]. The methodology and the results are reported for completeness. Monotonic tensile tests are performed on cylindrical specimens designed following EN13674-1 [16]. Following the extraction of the specimens from the head of the rail, these are maintained at a temperature of 200°C for six hours, to improve ductility and redistribute residual stresses at the surface that were possibly introduced during the machining procedure. A total of four specimens are extracted. The monotonic tensile tests are executed using an electro-mechanical universal testing machine INSTRON 5985 equipped with a load transducer having a nominal capacity of 250 kN. The tests are executed by controlling the displacement of the cross-head, translating at a constant speed of 0.75 mm/min which corresponds to a strain rate $\dot{\varepsilon}_L = 2.5 \times 10{-}4\ s^{-1}$, suitable for the determination of yield strength and elongation at fracture [16, 17]. Through the parallel length, the elongation is measured making use of a contactless extensometer measuring the relative displacement of two circular marks imprinted on the surface of the specimens at a distance of 50 mm. A frequency of 10 Hz is used to sample and save the applied force read by the load transducer and the elongation of the specimen.

Rotating bending tests

Rotating bending tests are executed on hourglass specimens designed according to ISO 1143:2021 [18]. The specimens are extracted from the head of the rail. The final surface finish is Ra=0.2 μm obtained at the lathe (circumferential machining). The diameter of the minimum cross-section is 7.0 mm. The tests are executed using an Italsigma RB35 rotating bending test machine. The load is applied through a linear electric actuator equipped with a 5 kN load transducer. The machine has a capacity of 35 Nm. The tests are executed at a rotational speed of 5000 rpm. The controller of the machine records the number of revolutions of the specimen and ensures that the applied load is stable within 1% range. The test is terminated at the fracture of the specimen when the applied load drops below 80% of the setpoint or after reaching either 5 10^6 or 10 10^6 cycles. After the fracture, the diameter of the rotating-bending specimens is measured using a Keyence VX5000 optical microscope. The obtained values are used to determine the stress in the calculation of the stress amplitude.

Fatigue crack growth rate

The tests aiming to quantify the fatigue crack growth rate are performed using compact tension C(T) specimens, with dimensions according to the ASTM-E647 [19]. Two specimens are extracted from the center of the rail head with the notch pointing downwards and having a thickness of B =10 mm and a width of W = 40 mm.

The tests have been executed in a testing frame equipped with a hydraulic actuator and a load cell with a nominal capacity of 125 kN. A closed-loop control system ensures that the test is controlled using force-feedback-loop. A clip-on displacement transducer - model UB-5A from TML - is mounted directly on the built-in knife edges manufactured at the crack mount with an initial opening of 4.0 mm. The specimen is loaded through clevis and pin, designed according to the aforementioned standards. In particular, the clevises have been manufactured with a flat-bottom hole, to reduce the influence of the pin-hole assembly on the compliance measurement. Moreover, both clevises are connected to the load line using spherical hinges, to ensure that secondary bending moments are minimized.

The data acquisition of the signals from the loadcell and extensometer is done with a controller having a sampling frequency of 2.5 kHz. The corresponding value of the force and the clip-on transducer are saved at the minimum and maximum load. The tests are conducted using two different load levels:

- Maximum force P_{max}=3.50 kN, and load ratio R=0.1;
- Maximum force P_{max}=4.50 kN, and load ratio R=0.5.

The cyclic loading is applied in a load control mode, at a constant load range, resulting in an increasing stress intensity factor range. During cyclic loading, the crack size is measured using the compliance method based on the crack mouth opening displacement which is measured with the clip-on extensometer. The compliance u, resulting from crack mount opening displacement v, is:

$$u = \left[\left(\frac{EvB}{P} \right)^{0.5} + 1 \right]^{-1} \tag{1}$$

where E is the Young's Modulus and P is the applied load [19]. The relative crack depth a is calculated as [19]:

$$\frac{a}{W} = 1.0010 - 4.6695\ \mathrm{u} + 18.460\ \mathrm{u}^2 - 236.82\ \mathrm{u}^3 + 1214.9\ \mathrm{u}^4 - 2143.6\ \mathrm{u}^5 \tag{2}$$

In addition, a visual inspection of the propagating crack has been used for calibrating the compliance, resulting in E=180 GPa.

Plane strain fracture toughness

The tests aiming to quantify the linear elastic plane-strain fracture toughness are performed using compact tension C(T) specimens, with dimensions according to the ASTM-E399 [20]. The specimen thickness and width are B = 20 mm and W = 40 mm, respectively. A fatigue pre-crack is induced in the specimens by applying constant amplitude loading characterized by a load ratio R=0.05 and P_{max}=8.6 kN. During the pre-cracking procedure, the crack size is monitored using the compliance measurement, as done for the crack growth rate test, and checked during the tests by using a hand-held microscope. Both the pre-cracking and the fracture toughness tests are done at room temperature.

The fracture toughness test is performed in a load-control setting by increasing the applied load at a constant rate up to fracture, such that the rate of the increase of the stress intensity factor is limited to 2.5 MPa $mm^{1/2}$ s^{-1}, following the standard

procedure. As a result of this, a crack mouth opening displacement versus load graph is obtained. This is analyzed following the procedure for determination of the size-insensitive fracture toughness, reported in *Annex X* of the ASTM-E399 [20]. In this procedure, the secant to the linear portion of the load-displacement graph is first identified. Successively the size-insensitive plane-strain fracture toughness K_{Isi}, is evaluated using a variable secant offset slope that is dependent on the size of the specimen uncracked ligament, *W-a*. For the C(T) specimen, the secant offset percentage is calculated as S_Q=100-106 /(W-a) [%], which is related to a 0.5 mm crack extension. This differs from the standard procedure where the secant offset percentage is fixed at 95%, corresponding to a 2% crack extension. This waives the condition for which the maximum load should be no larger than 1.1P_Q. In this way, since the plane-strain fracture toughness is measured at a fixed crack extension, the K_{Isi} is intended to be independent of the specimen size, opposite to K_{Ic}.
After the final fracture, the size of the fatigue pre-crack is measured with a Keyence VX5000 optical microscope. The crack size is measured according to the indications given in the ASTM E399, i.e. at the intersection with the free surfaces, at 25%, 50%, and 75% of the thickness, resulting in a total of 5 measurements per specimen. The average of the measurements is used as the pre-crack length, excluding the crack length at both free surfaces [20].

Vickers hardness

The rotating-bending specimens are sectioned along the longitudinal plane, using a water-cooled Struers Accutom-100. The samples are embedded in conductive Struers Polyfast resin, heated and pressed according to the specification of the producer, and consecutively ground with a series of SiC papers and polished up to 1 µm diamond paste before hardness testing.
Three lines of Vickers microhardness indentations, the centerline and close to both outer surfaces, were made with an indent spacing of d = 0.5 mm, to 10 mm from the fractured surface, to measure the hardness. The DuraScan 70 hardness tester applied a load of 10 N for 10 s. The samples are etched for 10 s with Nitric Acid diluted with ethanol (Nital) to 2%. Successively, high-magnification images of the microstructure are made, using a scanning electron microscope model Jeol 6500F, with a working distance of 10 mm, and an acceleration voltage of 20 kV.

Fractographic investigations

The fracture surfaces of all specimens, tensile, rotating bending, fracture toughness, and fatigue crack growth, are studied after intensive ultrasonic cleaning in isopropanol. For this purpose, a Jeol IT100 Scanning Electron Microscope (SEM) has been used with 15 kV acceleration voltage and 10 mm working distance in secondary electron imaging mode.
Additionally, the fatigue crack growth region of the fracture surface of the rotating bending specimen has been scanned with a Sensofar S Neox 3D optical profilometer to study the surface roughness. The surface is scanned in confocal mode, with standard 3D program settings with a 20x optic. For the analysis, the software package Sensoview v1.9.2 is used. The scans are cropped to have equal dimensions, with the initiation point, as observed in the propagation lines waving out, in the middle. The measurements are made directly on the raw data without smoothening. The average line roughness values are calculated from observations perpendicular to the crack growth direction, with a cut-off length, λ_c= 0.25 mm, and an evaluation length of 1.25 mm.

RESULTS AND DISCUSSION

Monotonic tensile tests

Fig. 1 depicts the uniaxial stress-strain curves measured during the monotonic tensile test of four R350HT specimens. It can be observed that up to the ultimate tensile stress, the curves coincide, denoting a high degree of reproducibility of the tests. When the stress exceeds the yield stress level, the strain hardening sets in, until the non-uniform deformation starts, resulting into necking. Tab. 2 summarizes the average properties measured in ref [15], in which the UTS is calculated as the maximum force divided by the specimen area.

Plane strain fracture toughness

The results of the experiments conducted to determine the linear elastic plane strain fracture toughness of R350HT at room temperature are summarized in Tab. 3. An average size-insensitive fracture toughness value of 1210 ± 20 MPa mm$^{0.5}$ is obtained from the valid tests, which is in line with typical values obtained for pearlitic rail steels [21].

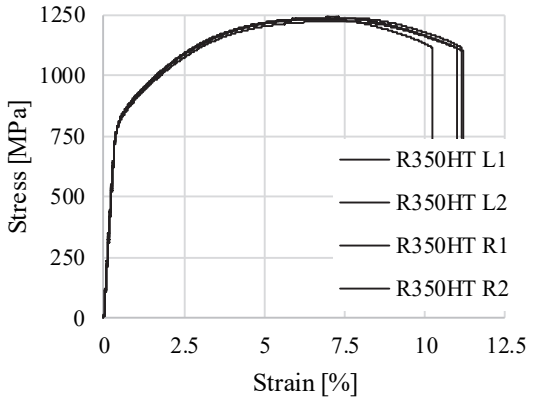

Figure 1: Monotonic engineering stress-strain curves, [15].

E [GPa]	$\sigma_{0.2,p}$ [MPa]	UTS [MPa]
219 ± 3.2	839 ± 4.2	1232 ± 3.8

Mean ± standard error, calculated as the ratio between the estimator of the standard deviation and the square root of the sample size.

Table 2: Average tensile properties.

Specimen	Precracking		Fracture Toughness Test		
	$Pmax$ [kN]	a [mm]	P_{Qsi} [kN]	P_{max} [kN]	K_{Isi} [MPa mm$^{0.5}$]
01	8.60	19.3	17.1	20.6	1237
02	8.60	20.2	15.8	18.7	1221
03	8.60	20.0	15.4	19.3	1172
				Average:	1210 ± 20[(a)]

(a) Mean ± standard error, calculated as the ratio between the estimator of the standard deviation and the square root of the sample size.

Table 3: Results of the linear elastic plane strain fracture toughness tests.

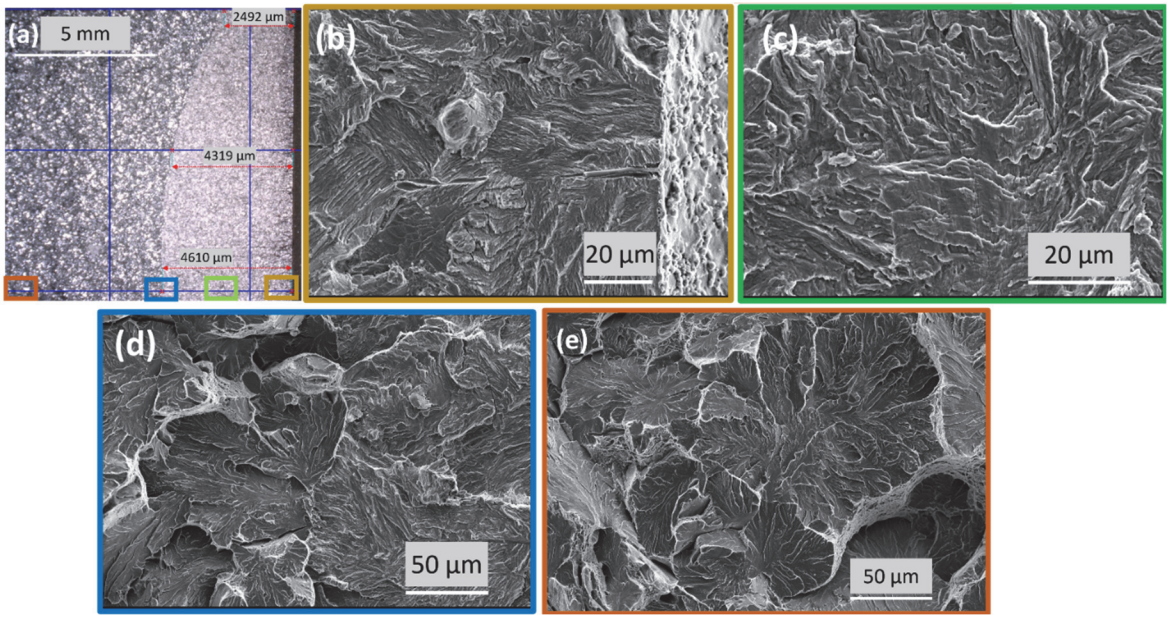

Figure 2: Fractography of the fracture toughness specimen 02; (a) Fatigue pre-crack zone and locations of the observations on the half width of the specimen, (b) one of the crack initiations from the notch produced by Electric Discharge Machining, (c) Fatigue pre-crack growth surface, (d) Transition from fatigue pre-crack to the final fracture region, (e) Final fracture region.

In Fig. 2 the characteristic features of the fractured surface are presented. Fig. 2(a) shows the half-width of specimen 02. A circular fatigue pre-crack zone and sharp transition to the brittle cleavage fracture surface are present. The grid lines with 5 mm spacing are placed to measure the fatigue pre-crack length at the previously indicated positions.
In Figs. 2(b)-(e) the fractography characteristics for the different stages of the test procedure are presented. The straight notch is produced with Electric Discharge Machining, resulting in the typical melted surface in Fig. (b). The same figure shows a crack initiation location in correspondence with an inclusion in the material. It is pointed out that several crack initiation points are recorded. The surface in Fig. 2(c) is the result of stable (fatigue) crack propagation, at half the total pre-crack length. Striations are present, perpendicular to the crack growth direction.
The fracture toughness test results in cleavage planes with river lines on them, as can be observed in Fig. 2(d), where the transition from pre-crack zone to cleavage fracture, is presented. With the crack extension, the cleavage planes increase in size as grains with low-angle grain boundaries are torn apart. Small ductile patches covered with micro-dimples are observed, these are associated with the rupture of the pro-eutectoid ferrite at the grain boundaries in the R350HT microstructure, as shown in Fig. 2(e).

Fatigue crack growth rate

The results of the fatigue crack growth rate tests are shown in Fig. 3. In particular, Fig. 3(a) shows the data produced in this study for both R=0.1 and R=0.5. The tests have been inferred with a Paris Law type of equation, i.e. $da/dn=C\Delta K^m$, to determine the fatigue crack growth rate coefficient and exponent. For R = 0.1 these are C = 1.13 10^{-15} and m = 3.81 and, for R = 0.5 these are C = 3.95 10^{-16} and m = 4.08, considering ΔK in [MPa mm$^{1/2}$], and da/dn in [mm/cycle].

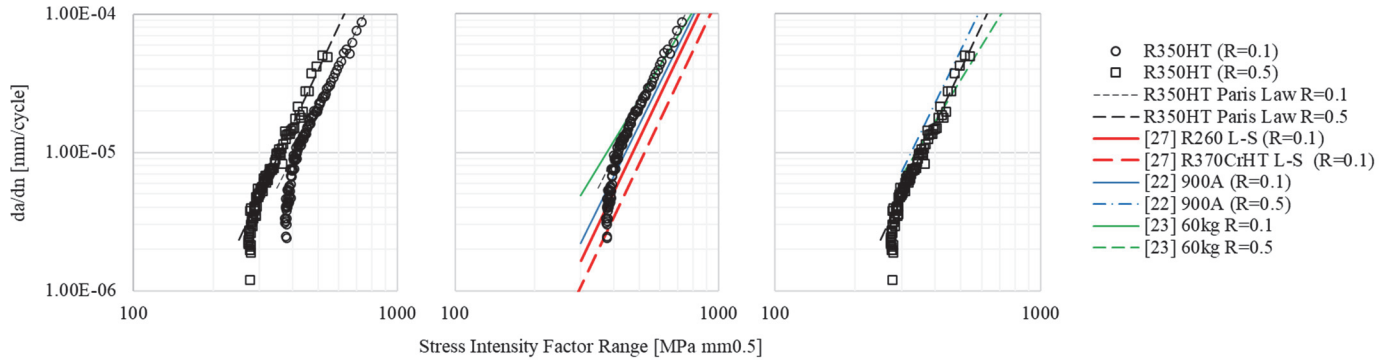

Figure 3: Results of the fatigue crack growth rate tests. (a) Results for R350HT steel tested in this study; (b) Comparison between R350HT and other pearlitic steels at R = 0.1; (c) Comparison between R350HT and other pearlitic steels at R = 0.5.

Figs. 3(b) and 3(c) show a comparison with the results of fatigue crack growth rate tests conducted in other studies on pearlitic steels for R = 0.1 and R = 0.5, respectively, like [23, 23, 27]. The comparison suggests that at a lower load ratio R the fatigue crack growth rate is more affected by the steel grade than at R = 0.5. Potentially, this can be attributed to plasticity-induced crack closure that is more prominent at low load ratios of which the extent is influenced by the yield stress of the material. It can be deduced that the fatigue crack growth rate for the tested R350HT steel is very similar to that of the grade 900A rail steel tested in [22] and of the R260 rail steel tested in [23], for both load ratios. R350HT shows a higher fatigue crack growth rate as compared to R260 rail steel, potentially indicating a lower damage-tolerant behavior of R350HT rails resulting from the difference in microstructure, although R260 and R350HT have very similar chemical compositions.
In Fig. 4 the fractography of the surface is presented for both load ratios, R = 0.1 and R = 0.5, paired by equal stress intensity factor ranges. The observations are made at 0.5B, the centerline of the fracture surface. In the figure, the crack propagation orientation is from right to left.
With the increase in crack length and stress intensity, the fatigue crack growth rate increases. For R = 0.1, this is a factor of approximately 9, between Fig. 4(a) and Fig. 4(c). At the fatigue crack growth surface of the latter, small well-defined cleavage zones are present. For R = 0.5, the crack length is longer before the same stress intensity factor range is reached, and the crack growth rate, da/dN, is higher for similar stress intensity factor ranges, as can be concluded from Fig. 3(a). The area fraction of brittle cleavage in Fig. 4(d) is, in line with these observations, larger, whereas at the low crack growth rate, Fig. 4(b), the fatigue crack growth is dominant.
When the crack propagates beyond the length in Fig. 4(c) and Fig. 4(d) a gradual transition from crack growth to unstable fracture is observed. The highest crack growth rate presented in Fig. 3(a), corresponds to a crack length of approximately 27 ± 0.5 mm for R = 0.1 and 25± 0.5 mm for R = 0.5. At these crack lengths, only a very small fraction of the surface area shows fatigue crack growth characteristics.

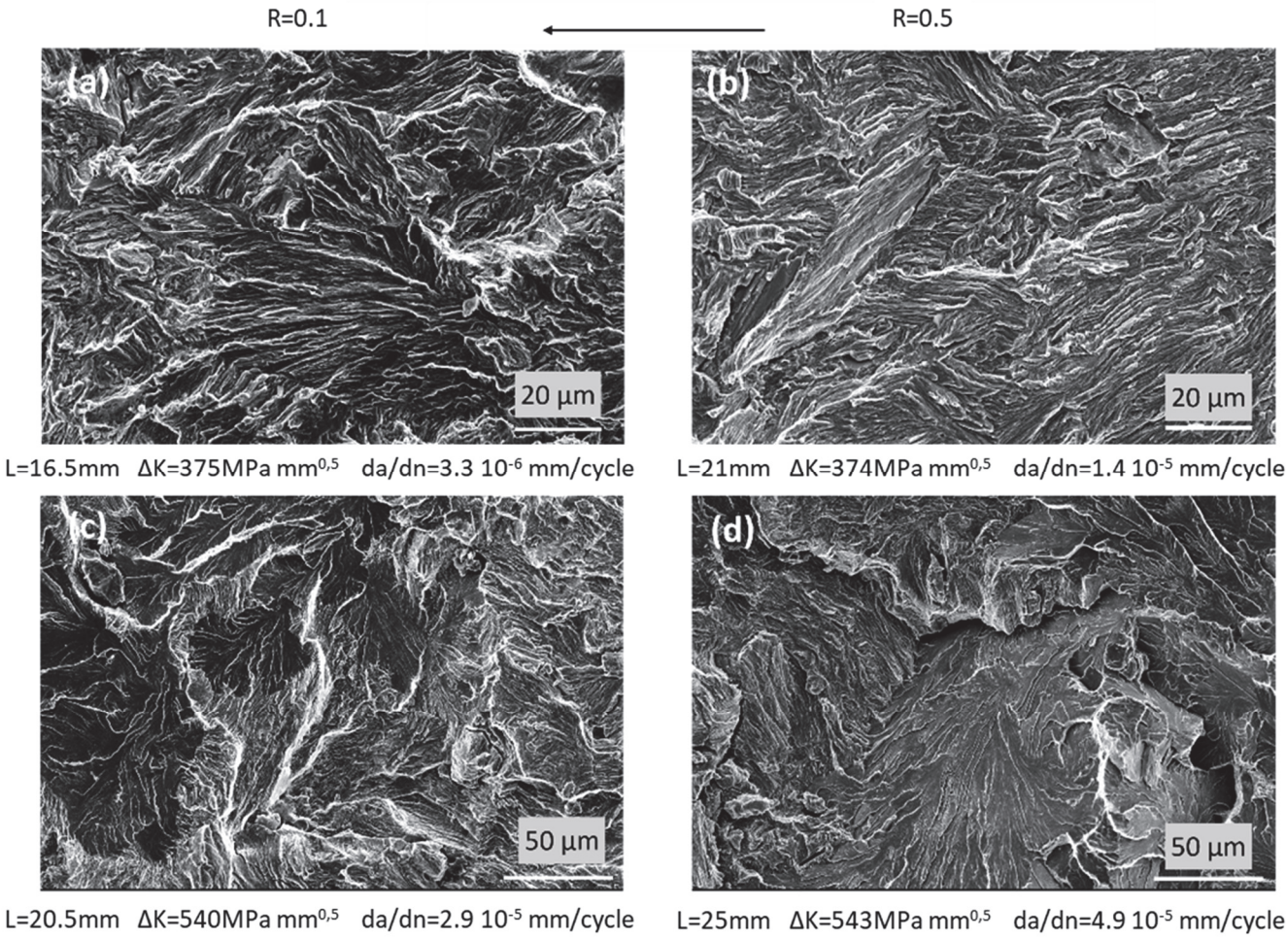

Figure 4: The surface characteristics of the fatigue crack growth specimen. Under each figure the crack length L, stress intensity factor range ΔK, and crack growth rate, da/dN, are presented. (a), (c), for the load ratio R = 0.1, and (b), (d), for R = 0.5.

Rotating bending

The results of the rotating bending tests (R = -1) are shown in Fig. 5, where the graph relates the number of cycles to test termination with the stress amplitude σ_a. In total, 11 specimens have been tested, resulting in 8 failed and 3 non-failed specimens. The failed test data have been inferred using a Basquin type of equation: $\log_{10}(N)=a_1+m_1\cdot\log_{10}(\sigma_a)$ [24]. It results that the median curve is characterized by a_1 = 24.1 and m_1 = -7.04, and the unbiased estimator for the standard deviation of the base 10 logarithm of the fatigue life, i.e. calculated considering 8-2=6 degrees of freedom, is $s_{\log10(N)}$=0.104. Below, Tab. 4 summarizes the test results.

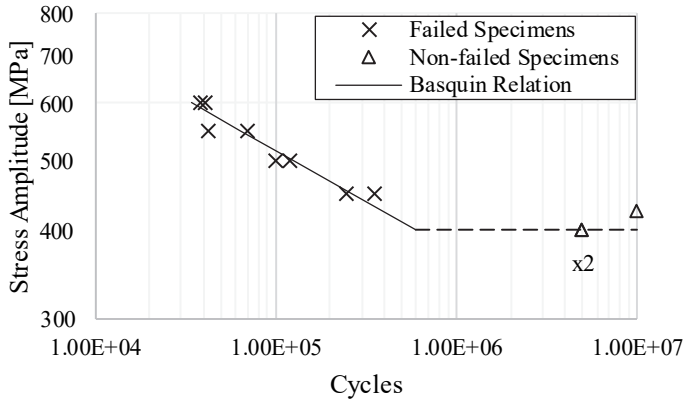

Figure 5: Rotating bending test results.

Specimen ID	σ_a [MPa]	Cycles	Failure 1=failure, 0=non failure
A1	600	40887	1
A2	600	38822	1
B1	400	5000000	0
B2	400	5000000	0
C1	550	70575	1
C2	550	42979	1
D1	500	100389	1
D2	500	120140	1
E1	450	351030	1
E2	450	247510	1
F1	425	10000000	0

Table 4: Rotating bending test data.

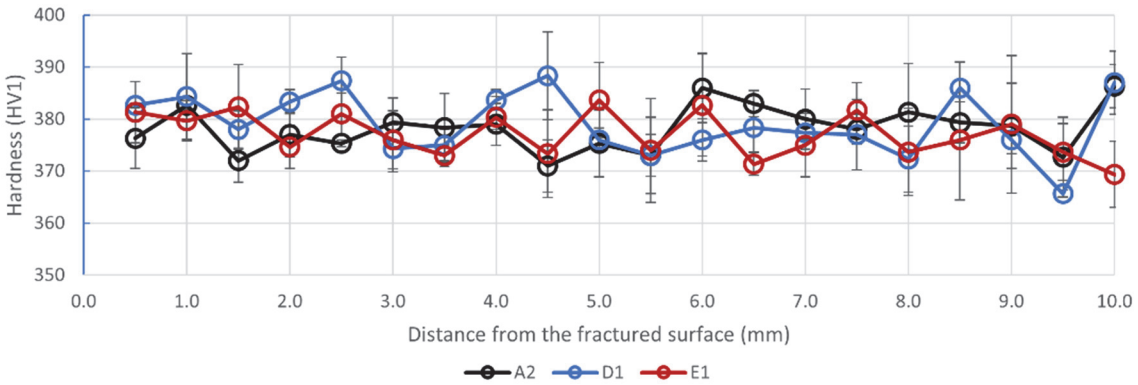

Figure 6: The hardness profile of the fractured rotating bending specimen at different stress levels; A: 600 MPa, D: 500 MPa, E: 450 MPa.

The hardness of the rotating bending specimen is sampled in a longitudinal section obtained from a failed specimen, to a distance from the fractured surface of 10 mm, see Fig. 6. No hardness increase is observed close to the fractured surface. The results suggest that no macroscopic plastic deformation takes place in the vicinity of the fracture surface, which can be explained by the specimen shape and the fatigue load being lower than the yield stress. The cross-section area of the hourglass-shaped specimen increases at short distance next to the smallest diameter area, with a decrease in stress as result. The fracture surfaces are characterized by multiple fatigue crack propagation zones with cracks initiating at the free surface of the specimens and a brittle final fracture zone in the central region. Fig. 6(a) shows an optical microscopy image of specimen D1. It appears that two semi-round short crack planes with a length of approximately L = 0.65 ± 0.02 mm are present on one side and on the opposite side a longer fatigue crack with a depth of about 2.3 ± 0.2 mm. In the plane of the longer crack, a step is present, as indicated by the arrow.

On the fracture surface, the distribution and the number of cracks along the free surface vary per tested specimen. Despite this, in all 8 specimens that failed, a single fatigue crack propagates to cover a relatively large area. For the shorter cracks, a clean initiation and growth pattern is visible, as presented in Fig. 6(b). The initiation area shows a dense pattern and waves out next to it. Areas depicting both are indicated. Also at the larger cracks, a clear initiation and growth pattern is observed,

especially close to the initiation location. For larger crack sizes, the surface shows more brittle features and clear propagation lines tend to diminish.

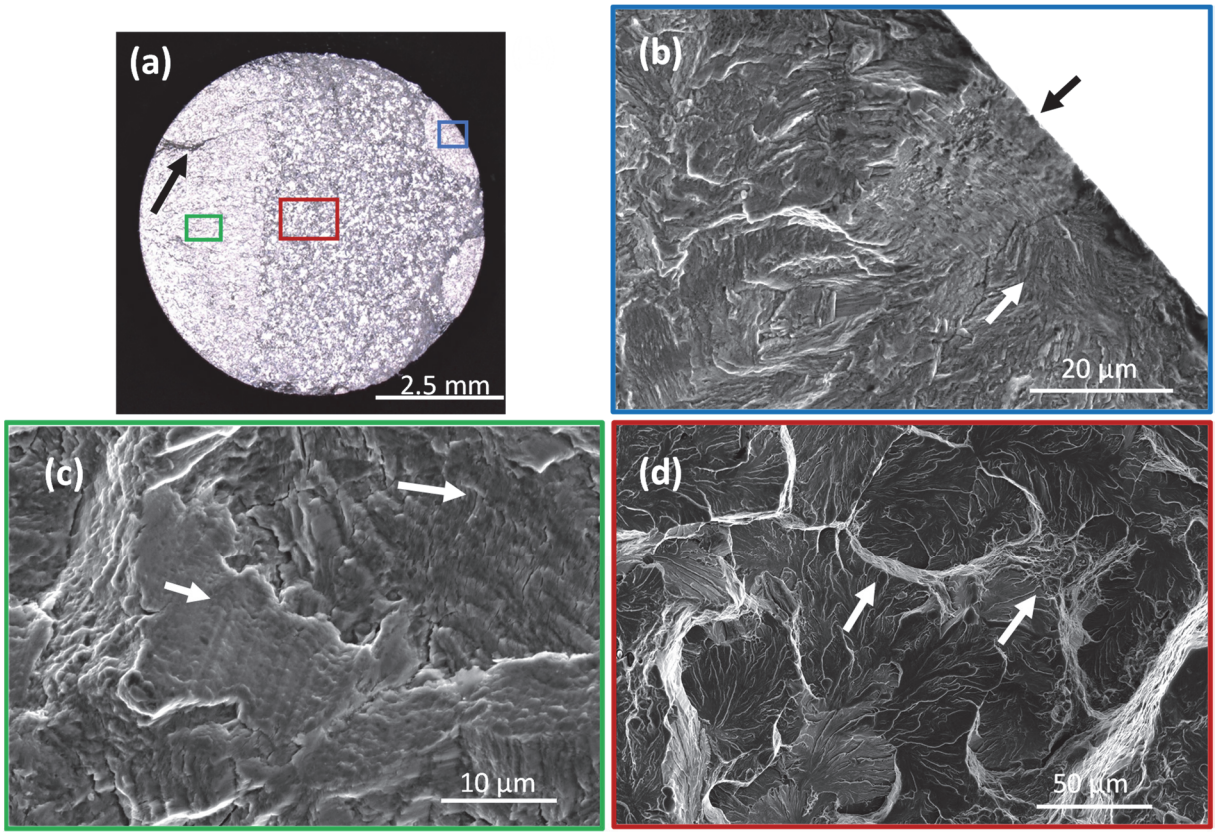

Figure 6: Characteristics of crack growth and final fracture, specimen A4; (a) optical microscopy image of the fracture, (b) fatigue crack initiation at the circumference, (c) fatigue crack growth pattern and the effect of crack closure, (d) final fracture.

Due to the load ratio R =-1, every location in the test section experiences a transition from tensile to compressive stress during each rotation. During the compression, the crack surfaces are pressed together resulting in local contact, which causes local deformation. At the fracture surface of specimens tested at the higher stress levels, only a limited area is deformed. With a decreasing stress level and, as a consequence, an increasing number of revolutions an increasing area fraction is smoothened by the repetitive crack closure. The area fraction that is deformed further decreases with the crack length.

In Fig. 6(c) the resulting surface is presented, positioned within the green frame, at the midpoint of the fatigue crack. The fatigue striations are visible, especially on the smooth surface, smoothened and extruded during the repetitive crack opening-closing, but also next to these zones. Generally, the distance between the striations confirms that the fatigue crack growth rate is relatively high, i.e. the resulting contribution of stable crack propagation to the total fatigue life experienced by the specimens is negligible. The final fracture region is a brittle cleavage fracture. The resulting surface is presented in Fig. 6(d), although small zones of ductile fracture are visible, as pointed by the arrow.

The fatigue crack growth zone of three samples with an increasing number of revolutions to fracture are scanned with a Sensofar optical profilometer and then analyzed. The height profile of the scanned area of sample A2 is presented in Fig. 7. Then the surface roughness has been calculated at equal distances to the free surface. It is observed that with the distance the surface roughness increases. For all three specimens, the roughness increases with the crack length, and also in order of the total number of rotations. The highest roughness values are observed at the specimen with the lowest number of rotations until fracture.

It is known for pearlitic steel that, at low stress, the crack path follows the colony boundary until, at higher stress, the crack path straightens and cuts through the lamellae [25, 26]. In specimen E1, the crack path and microstructural deformation are observed at the surface of the longitudinal section, both close to the fractured surface and at a secondary crack that is present close to the fracture plane.

The secondary crack propagates parallel to the final fracture surface and shows multiple kinks, before branching to propagate virtually straight towards the fracture surface, Fig. 8(a). At the crack flanks, the microstructure is deformed and compressed

as a result of the crack closure effect to a depth of approximately 1 μm, Fig. 8(b). At the fractured surface, comparable deformation patterns are observed. At the onset of the brittle final fracture, deformation is observed as indicated in Fig. 8(c), although the crack propagation direction is perpendicular to the lamellar orientation.

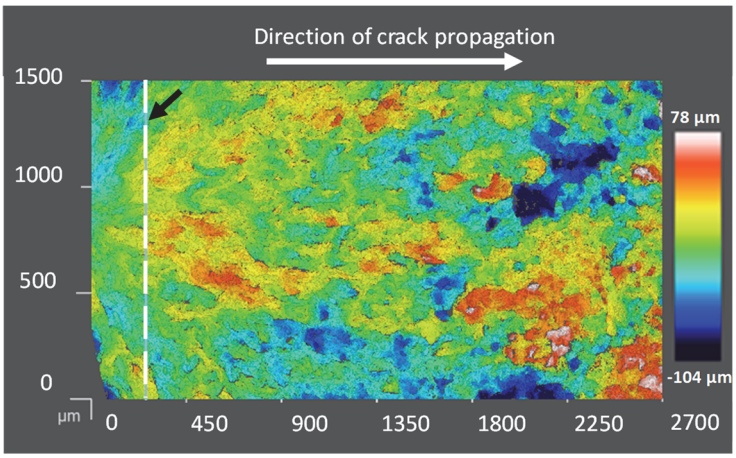

Figure 7: The surface scan of sample A2. The vertical line indicates one of the positions to calculate the roughness.

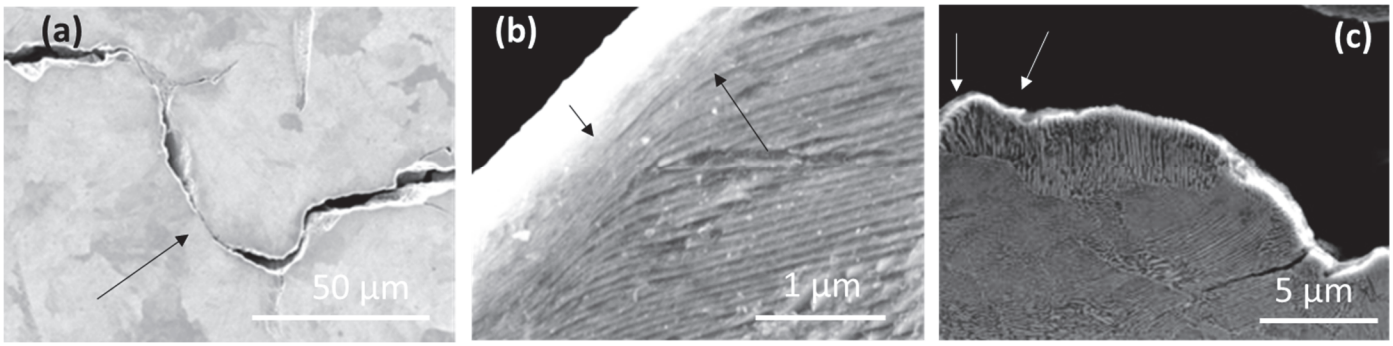

Figure 8: The crack path in the rotating bending specimen E1; (a) the crack path of the secondary crack; (b) deformation as a result of closure in the secondary crack; (c) fracture surface at the central region of the specimen, close to the final cleavage fracture.

Conclusions

The following conclusions can be drawn from this experimental investigation of the fatigue and fracture resistance of R350HT:

- The study provides a characterization of fatigue and fracture mechanics properties of R350HT fine pearlitic rail steel executed at room temperature.
- The characteristic crack closure effect in the rotating bending test results in deformed contact patches at the fractured surface. It is observed that the area fraction of these contact patches is largest at the fractured surface of those specimens that endured the lowest stress amplitude. It is further observed that the area fraction decreases with the increase of the surface roughness.
- The surface of the fatigue crack growth specimen evolves gradually from fatigue growth to cleavage fracture. No sudden transition between stable and unstable crack propagation is observed. Already at low stress intensity fracture range lamellar tearing is observed by the terrace steps at the surface. The area fraction and dimensions of these cleavage planes increase with increasing ΔK.
- At comparable stress intensity factor ranges, the crack growth rate is higher for the $R = 0.5$ load ratio. Cleavage planes are wider whereas the small, well-defined, cleavage planes are present at the fracture surface for the $R = 0.1$ load ratio.
- With the increase in crack length the dimension of the cleavage planes increases as well. The low-angle grain boundaries do not slow crack growth down as the fracture energy increases.

DATA AVAILABILITY

The data are available on request.

DECLARATION OF COMPETING INTEREST

The authors declare no competing interest.

ACKNOWLEDGEMENT

The research contribution of B. Schotsman was carried out under project number T18014 in the framework of the Partnership Program of the Materials innovation institute M2i (www.m2i.nl). Robert Jan Meijer, at the University of Twente, Department of Mechanics of Solids, Surfaces & Systems is acknowledged for the access and use of the optical profilometer. The authors would like to thank Voestalpine Track Solutions Netherlands for providing the rail steel for this research.

REFERENCES

[1] Zerbst, U., Lundén, R., Edel, K. O. and Smith, R. A. (2009). Introduction to the damage tolerance behaviour of railway rails–a review. Engineering fracture mechanics, 76(17), pp. 2563-2601. DOI: 10.1016/j.engfracmech.2009.09.003
[2] Pucillo, G. P., De Iorio, A., Rossi, S. and Testa, M. (2018). On the effects of the USP on the lateral resistance of ballasted railway tracks. In ASME/IEEE Joint Rail Conference, 50978, p. V001T01A017. American Society of Mechanical Engineers. DOI: 10.1115/JRC2018-6204
[3] Christoforou, P., Fletcher, D. I. and Lewis, R. (2019). Benchmarking of premium rail material wear. Wear, 436, 202990..
[4] Kapoor, A. (1997). Wear by plastic ratchetting. Wear, 212(1), pp. 119-130. DOI: 10.1016/j.wear.2019.202990
[5] Zerbst, U., Mädler, K. and Hintze, H. (2005). Fracture mechanics in railway applications—an overview. Engineering fracture mechanics, 72(2), pp. 163-194. DOI: 10.1016/j.engfracmech.2003.11.010
[6] Pucillo, G. P. (2022). The effects of the cold expansion degree on the fatigue crack growth rate in rail steel. International Journal of Fatigue, 164, 107130. DOI: 10.1016/j.ijfatigue.2022.107130
[7] Olzak, M., Stupnicki, J. and Wojcik, R. (1991). Investigation of crack propagation during contact by a finite element method. Wear, 146(2), pp. 229-240. DOI: 10.1016/0043-1648(91)90065-3
[8] Bogdanski, S., Olzak, M. and Stupnicki, J. (1996). Numerical stress analysis of rail rolling contact fatigue cracks. Wear, 191(1-2), pp. 14-24. DOI: 10.1016/0043-1648(95)06685-3
[9] Trollé, B., Gravouil, A., Baietto, M. C. and Nguyen-Tajan, T. M. L. (2012). Optimization of a stabilized X-FEM formulation for frictional cracks. Finite elements in analysis and design, 59, pp. 18-27. DOI: 10.1016/j.finel.2012.04.010
[10] Pucillo, G. P., Carrabs, A., Cuomo, S., Elliott, A. and Meo, M. (2021). Cold expansion of rail-end-bolt holes: Finite element predictions and experimental validation by DIC and strain gauges. International Journal of Fatigue, 149, 106275. DOI: 10.1016/j.ijfatigue.2021.106275
[11] Leonetti, D. and Vantadori, S. (2022). Weight functions for stress intensity factor and T-stress derived for an inclined edge crack in a finite width plate. International Journal of Fatigue, 165, 107170. DOI: 10.1016/j.ijfatigue.2022.107170
[12] Leonetti, D. and Vantadori, S. (2022). On the growth of rolling contact fatigue cracks using weight functions. Procedia Structural Integrity, 39, pp. 9-19. DOI: 10.1016/j.prostr.2022.03.067
[13] Rosenfield, A. R., Hahn, G. T. and Embury, J. D. (1972). Fracture of steels containing pearlite. Metallurgical and Materials Transactions B, 3, pp. 2797-2804. DOI: 10.1007/BF02652845

[14] Masoudi Nejad, R., Farhangdoost, K. and Shariati, M. (2020). Microstructural analysis and fatigue fracture behavior of rail steel. Mechanics of Advanced Materials and Structures, 27(2), pp. 152-164. DOI: 10.1080/15376494.2018.1472339
[15] Leonetti, D., Ferreira, V. M. and Schotsman, B. (2023). Fracture behavior and mechanical characterization of R350HT rail steel. Procedia Structural Integrity, 47, pp. 219-226. DOI: 10.1016/j.prostr.2023.07.015
[16] EN 13674-1 (2011). Railway applications - Track - Rail - Part 1: Vignole railway rails 46 kg/m and above.
[17] ISO 6892-1 (2019). Metallic materials - Tensile testing - Part 1: Method of test at room temperature.
[18] ISO 1143 (2021). Metallic materials - Rotating bar bending fatigue testing.
[19] ASTM E647-23a (2023). Standard Test Method for Measurement of Fatigue Crack Growth Rates
[20] ASTM E399-22 (2022). Standard Test Method for Linear-Elastic Plane-Strain Fracture Toughness of Metallic Materials
[21] De Iorio, A., Grasso, M., Penta, F. and Pucillo, G. P. (2013). About the certification of railway rails. Frattura ed Integrità Strutturale, 7(26), pp. 57-68. DOI: 10.3221/IGF-ESIS.26.07
[22] Christodoulou, P. I., Kermanidis, A. T. and Haidemenopoulos, G. N. (2016). Fatigue and fracture behavior of pearlitic Grade 900A steel used in railway applications. Theoretical and Applied Fracture Mechanics, 83, 51-59. DOI: 10.1016/j.tafmec.2015.12.017
[23] Kim, J. K. and Kim, C. S. (2002). Fatigue crack growth behavior of rail steel under mode I and mixed mode loadings. Materials Science and Engineering: A, 338(1-2), pp. 191-201. DOI: 10.1016/S0921-5093(02)00052-7
[24] Basquin, O. (1910). The exponential law of endurance tests. In Proc Am Soc Test Mater, 10, pp. 625-630.
[25] Daeubler, M. A., Thompson, A. W. and Bernstein, I. M. (1990). Influence of microstructure on fatigue behavior and surface fatigue crack growth of fully pearlitic steels. Metallurgical Transactions A, 21, pp. 925-933. DOI: 10.1007/BF02656577
[26] Park, Y. J. and Bernstein, I. M. (1979). The process of crack initiation and effective grain size for cleavage fracture in pearlitic eutectoid steel. Metallurgical Transactions A, 10, pp. 1653-1664. DOI: 10.1007/BF02811698
[27] Maya-Johnson, S., Ramirez, A. J. and Toro, A. (2015). Fatigue crack growth rate of two pearlitic rail steels. Engineering fracture mechanics, 138, pp. 63-72. DOI: 10.1016/j.engfracmech.2015.03.023